Experimental research on mechanical behavior of UHPCFST under repeat axial compression

Chunlei Yu[a], Min Yu[a*], Lihua Xu [a],Sumei Liu [a],Tan Wang [a], Jianqiao Ye[b]

[a] School of Civil Engineering, Wuhan University, Wuhan 430072, China

[b] School of Engineering, Lancaster University, Lancaster LA1 4YR. UK

Abstract: This paper investigates the mechanical behavior of ultra-high performance concrete-filled steel tubes (UHPCFST) subjected to repeated axial compression. A total of 34 specimens of UHPCFST were systematically designed, constructed, and evaluated experimentally. The design parameters encompassed steel tube wall thickness, UHPC type, specimen size (varying diameters while preserving a consistent diameter-to-thickness ratio), and loading scheme. The failure patterns, stress-strain relationships, axial load-bearing capacity, and stiffness were meticulously examined. Predominantly, shear failure and drum-shaped upsetting failure were identified as the primary failure mechanisms in the specimens. The axial load-bearing capacity was found to increase notably with the use of thicker steel tubes and higher-grade UHPC. Under repeated loading, a reduction in stiffness was noted, which was dependent on factors such as the steel content, tube diameter, and the volume of coarse aggregate of UHPC. Current predictive equations for the axial load-bearing capacity of CFST were assessed using the experimental results of UHPCFST and were determined to over-predict the axial load-bearing capacity of UHPCFST. Consequently, a refined equation is proposed to yield a more precise estimation of the axial load-bearing capacity for UHPCFST. Furthermore, an empirical model was developed to characterize the stress-strain behavior of UHPCFST under repeated axial compression,

offering a tool for practical engineering design and analysis.

Keywords: UHPCFST, mechanical behavior, repeat axial compression

1. Introduction

A Concrete-Filled Steel Tube (CFST) is a composite structure comprising a steel tube filled with concrete. This composite structure is extensively utilized in structural engineering due to its exceptional strength, stiffness, and ductility. The synergy of steel and concrete within a CFST enhances the concrete's compressive strength and ductility by providing confinement. CFSTs have been broadly implemented in various applications, including bridge piers, columns, and offshore structures.[1,2]. Despite their advantages, the use of normal concrete (NC) in CFSTs necessitates larger cross-sections, which may lead to increased structural weight, reduced space efficiency, construction complexities, and potential aesthetic limitations. An alternative to NC is Ultra-High Performance Concrete (UHPC), a novel construction material that surpasses NC, high-strength concrete, and high-performance concrete in terms of compressive strength and durability[3,4]. However, UHPC exhibits greater brittleness[5,6] than NC, which can diminish deformability and energy absorption before failure. The integration of UHPC in CFSTs (UHPCFSTs) can solve the brittleness issue[7] and enhance load-bearing capacity and mechanical properties while potentially reducing structural weight by up to 50% compared to NC counterparts[8]. As a result, UHPCFSTs represent a highly promising and innovative advancement in composite structural forms, with significant potential to shape the future of construction and engineering[9].

Recently, diagrid structures incorporating CFST components have garnered increasing attention for their application in diverse fields, including the cooling towers of power plants [10–12]and high-rise buildings[13]. Diagrid structures are utilized to augment the lateral stiffness of the structure system and fulfill the criteria for seismic design. [14] Diagrid structures possess the capability to convert horizontal forces into axial forces that are then sustained by CFST components. As a result, CFST components are prone to repeated axial loads during seismic events[15,16]. Thus, it is of practical significance to examine the mechanical behavior of CFST under repeated axial loads. Although extensive research[17,18] has been conducted on the mechanical behavior of CFST under monotonic axial compression since the last century, resulting in design formulas that are adopted in Chinese codes[19,20] to calculate the bearing capacity of CFST, there is a relative scarcity of studies on the mechanical properties of CFST under repeated axial compression[21]. This research gap is primarily due to the limited application of this loading condition. Similarly, the mechanical performance of UHPCFST, which shows promise as a potential replacement for CFST, also lacks sufficient investigation in this aspect. To facilitate future applications of UHPCFST, it is imperative to conduct studies on the mechanical behavior of UHPCFST under repeated compression loads.

This study experimentally investigates the compressive performance of UHPCFST to address the previously identified research gap. To exclude global buckling in this study and focus on the sectional strength of the UHPCFSTs, thirty-four stub UHPCFST specimens are tested under either monotonic or repeated compressive loading to examine their mechanical behavior. The study detailly examines failure modes, bearing capacity, compressive stiffness, and stiffness degradation of the UHPCFST under repeated axial compression. Existing code provisions and formulas for calculating bearing capacity are evaluated. An exponential decay formula and a three-phase mathematical model are proposed to predict, respectively, the stiffness degradation and the relationship between axial strain and force in the UHPCFST under repeated axial compression.

2. Experimental program

2.1. Specimen design

Thirty-four UHPCFST specimens are tested to investigate the mechanical behavior of the UHPCFST subjected to axial compression. Three different types of UHPC, each of which contains a different volume fraction of coarse aggregate, seven different steel tubes are used to fabricate the UHPCFST specimens for compressive experiments. To investigate compressive stiffness degradation of the UHPCFST under compressive loading, the specimens are divided into two groups of the same number, *i.e.*, seventeen of the specimens are for monotonic compression test and the other seventeen are for repeated compression test. The design details of the thirty-four specimens are shown in Table.1. The outer diameters of the steel tubes are 108mm, 168mm, and 219mm, respectively. The height of each specimen is three times its diameter for avoiding stability issue. Four different steel thickness, *i.e.*, 4mm, 6mm, 8mm and 10mm, are considered to evaluate the effect of steel confinement. The coarse aggregate volume fractions are, respectively, 0, 15% and 30%. It is worth noting that the size effect can be investigated by simultaneously changing the diameter and thickness of the steel tube while keeping the ratio between them constant.

Table.1 Design parameters of specimen

No	Specimen label	D × T × L (mm)	V_{ca} (%)	f_y (MPa)	f_{cu} (MPa)	α	ξ
1/2	D108T4CA00-M/R	$108 \times 4 \times 324$	0	415	125	0.166	0.684
3/4	D108T4CA15-M/R	$108 \times 4 \times 324$	15	415	134	0.166	0.606
5/6	D108T4CA30-M/R	$108 \times 4 \times 324$	30	415	142	0.166	0.535
7/8	D108T6CA00-M/R	$108 \times 6 \times 324$	00	412	125	0.266	1.084
9/10	D108T6CA15-M/R	$108 \times 6 \times 324$	15	412	134	0.266	0.960
11/12	D108T6CA30-M/R	$108 \times 6 \times 324$	30	412	142	0.266	0.848
13/14	D108T8CA00-M/R	$108 \times 8 \times 324$	0	406	125	0.378	1.520
15/16	D108T8CA15-M/R	$108 \times 8 \times 324$	15	406	134	0.378	1.346
17/18	D108T8CA30-M/R	$108 \times 8 \times 324$	30	406	142	0.378	1.190
19/20	D168T6CA00-M/R	$168 \times 6 \times 504$	00	450	125	0.160	0.712
21/22	D168T6CA15-M/R	$168 \times 6 \times 504$	15	450	134	0.160	0.631
23/24	D168T6CA30-M/R	$168 \times 6 \times 504$	30	450	142	0.160	0.557
25/26	D168T8CA15-M/R	$168 \times 8 \times 504$	15	374	134	0.222	0.727
27/28	D168T10CA15-M/R	$168 \times 10 \times 504$	15	401	134	0.289	1.015
29/30	D219T8CA00-M/R	$219 \times 8 \times 657$	15	360	125	0.164	0.584
31/32	D219T8CA15-M/R	$219 \times 8 \times 657$	15	360	134	0.164	0.517
33/34	D219T8CA30- M/R	$219 \times 8 \times 657$	15	360	142	0.164	0.457

In Table.1, D, t and L denote, respectively, outside diameter, thickness and length of a steel tube; V_{ca} is coarse aggregate volume fraction of concrete; f_{cu} is cubic compressive strength of UHPC; f_y is yield strength of steel; α is steel ratio, for circle section, α=4t/d; ξ is confinement factor[22]. The specimens to be tested are labeled with DiTiCAjk-L, where Di denotes diameters of $i$mm, Ti denotes thickness of $i$mm, CAjk denotes coarse aggregate volume fraction of jk% and L takes M for monotonic loading and R for repeated loading, respectively.

2.2. Materials properties

The mechanical behavior of UHPCFST is influenced by the properties of both the steel tube and the UHPC. Therefore, it is crucial to conduct experiments to obtain the basic mechanical properties of these two materials.

Following the previous researches[23–25] and guidelines of the Chinese code GB/T 228.1:2010[26], steel coupons are made from the seamless steel tubes as the test samples, as shown Fig.1 and Fig.2. The geometrical dimensions of the coupons are presented in Table.2.

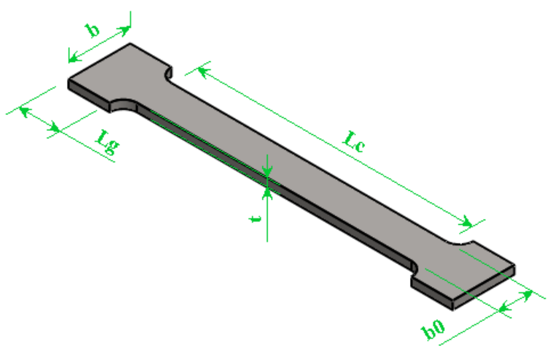

Fig.1. Dimension of the steel tube test coupons

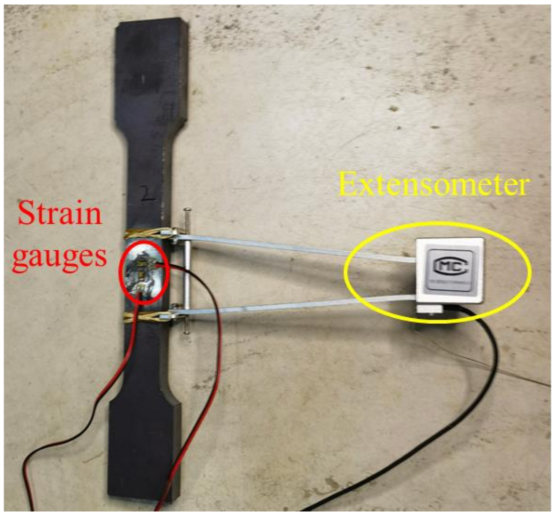

Fig.2. Photo of steel coupon

The curved steel sample in Fig.2 is extracted from a steel tube of the UHPCFST studied in this paper. Tensile tests are performed using a 60T tension-compression quasi-dynamic testing machine in the laboratory of Structural Engineering at Wuhan University. To apply the tensile force, the top and the bottom ends of the sample are flattened and clamped by the loading machine as shown in Fig.3,

Table.2 Geometry of steel tube test samples

Sample label	Steel tube dimension D×t× L (mm)	L_c (mm)	L_g (mm)	b0 (mm)	B (mm)
S1	$108 \times 4 \times 324$	80	30	25	35
S2	$108 \times 6 \times 324$	90	30	25	35
S3	$108 \times 8 \times 324$	110	30	25	35
S4	$168 \times 6 \times 504$	90	30	25	35
S5	$168 \times 8 \times 504$	110	30	25	35
S6	$168 \times 10 \times 504$	120	30	25	35
S7	$219 \times 8 \times 657$	130	40	38	58

In Table.2, D, t and L denote, respectively, outside diameter, thickness and length of a steel tube. L_c, L_g, b0 and B are steel coupons dimensions that are defined in Fig.1

The applied force is measured by the force sensor of the testing machine. As seen in Fig.2 and Fig.3, extensometer and strain gauges are both use to measure the strains. The extensometer is used to record vertical strain of the sample, and the strain gauges are used to record both horizontal and vertical strain of the sample to calculate Poisson's ratio. Displacement loading control is employed during the test, with a loading rate of 0.5mm/min.

Fig.3. Test set-up

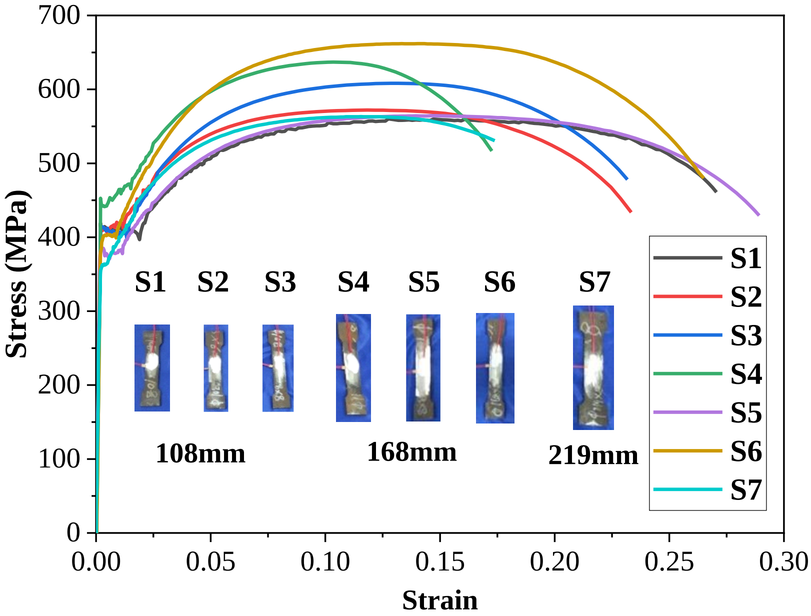

Fig.4. Stress-strain curve of steel tube samples

All the tests exhibit tensile fracture at the center of the specimens as the predominant failure mode. The stress-strain curves of the samples are illustrated in Fig.4. Noticeable yield plateaus are found in the stress-strain curves. Table.3 presents the yield strength, ultimate strength, elastic modulus and Poisson's ratio of the tested steel coupons.

Table.3 Properties of steel tube

Sample Label	Seamless steel tube diameter (mm)	Thickness (mm)	Yield stress (MPa)	Ultimate stress (MPa)	Elastic module (GPa)	Poisson's ratio
S1		4	415	560	210	0.30
S2	108	6	412	570	196	0.28
S3		8	406	610	199	0.29
S4		6	450	636	209	0.30
S5	168	8	374	564	210	0.31
S6		10	401	661	208	0.28
S7	219	8	360	563	203	0.30

Three mixtures of the UHPC are applied to investigate the effect of coarse aggregate volume fraction on the compressive behavior of UHPCFST. The details of the mixtures are provided in Table.4. The concrete binder consists of P.O.52.5 cement, silica fume with 95% Si content, and fly ash. Polypropylene fibers with a diameter of 18-48 μm and straight copper-coated steel fibers measuring 13 mm in length and 0.2 mm in diameter are added to the mixture. Highly effective polycarboxylate superplasticizer powders are used to enhance the fluidity of the fresh mixture. The UHPC incorporates quartz sand with a particle size of 69-178 μm as the fine aggregate and basalt with a size range of 5-10 mm as the coarse aggregate. Based on the recommendations from the previous research[27,28], three coarse aggregate volume fractions, namely 0%, 15%, and 30% (referred to as CA00, CA15, and CA30, respectively) and 2% steel fiber volume fraction are selected to ensure both strength and workability of the UHPC.

Table.4 Mixture of UHPC (kg/m^3)

UHPC	Cement	Silica fume	Fly ash	Water	Quartz sand	Coarse Aggregate	Super plasticizer	Steel fiber	Polypropylene fiber
UHPC-CA00	857	107	107	182	1179	-	11.8	157 (2%)	1.9 (0.2%)
UHPC-CA15	725	91	91	154	998	375 (15%)	10	157 (2%)	1.9 (0.2%)
UHPC-CA30	594	74	74	126	817	750 (30%)	8.2	157 (2%)	1.9 (0.2%)

According to the Chinese Code T/CCPA 35—2022[29], cubic samples (100mm x 100mm x 100mm) are fabricated to measure the cubic compressive strength of the UHPC cubes. Additionally, cylinder samples measuring 100mm in diameter and 200mm in height are made to measure the cylinder compressive strength and elastic modulus of the UHPC. The measured mechanical properties are presented in Table.5.

Table.5 Mechanical Properties of UHPC

UHPC	Cubic compressive strength (MPa)		Cylinder compressive strength (MPa)		Elastic module (GPa)	
	28^{th} day	Test day	28^{th} day	Test day	28^{th} day	Test day
UHPC-CA00	126	129	101	103	47	48
UHPC-CA15	135	138	114	118	48	50
UHPC-CA30	143	145	129	132	51	51

2.3. Test set-up and load patterns

The compressive experiments on the UHPCFST are conducted in the laboratory of Structural Engineering at Wuhan University using a shear-compression test loading machine with a maximum compression capacity of 30000kN. The deformation of the specimens is measured using two Linear Variable Differential Transformers (LVDTs). Additionally, two pairs of vertical and horizontal strain gauges are attached to the middle of the specimen to measure the real-time vertical and horizontal strain of the steel tube. One side of the surface of the steel tube is painted white with a black grid, which helps visualizing the deformation of the specimens during loading and at the final failure. The schematic diagram and a photo of the test can be found in Fig.5.

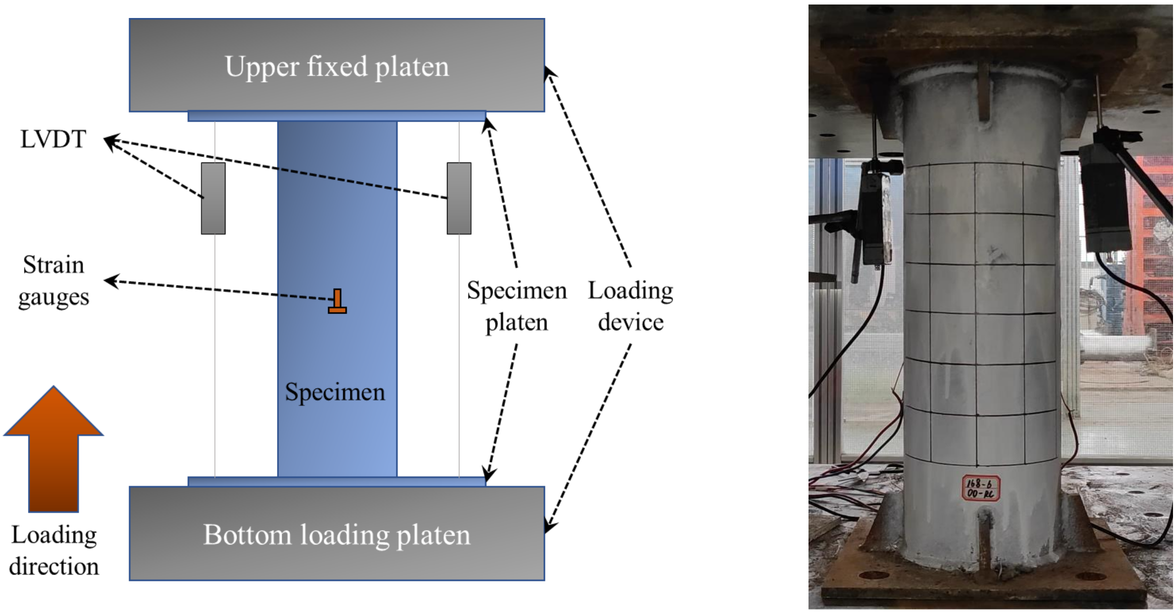

a). Schematic diagram **b).** Photo of the test

Fig.5. Test set-up

Two different loading patterns, namely monotonic compression and repeated compression, are applied in the experiments. Displacement-controlled loading is implemented with variable loading rates and increments per round (Fig.6). In the case of monotonic compression, a constant loading rate of 1 mm/min is applied until the displacement reaches one-tenth of the specimen height. For the repeated compression tests, a loading rate of 1 mm/min and a displacement increment per loading round of 1/333 of the specimen height are applied until the specimen yields. Subsequently, the loading rate is increased to 2 mm/min and the displacement increment per loading cycle is increased to 1/100 of the specimen height until the displacement reaches one-tenth of the specimen height.

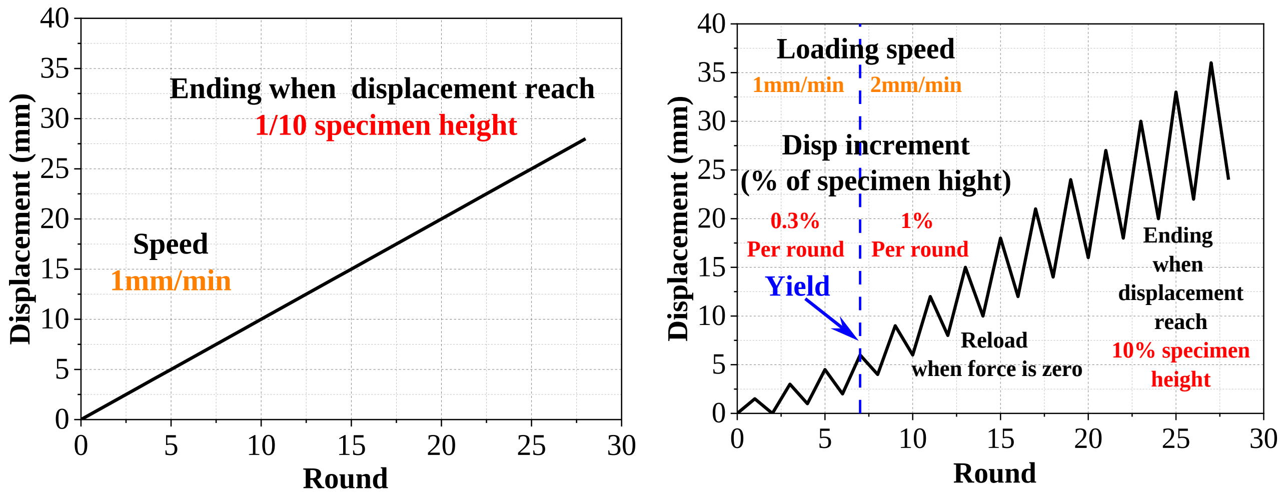

a). Monotonic compression **b).** Repeated compression

Fig.6. Displacement-controlled Load patterns

3. Test result

3.1. Failure mode

The outer steel tubes were removed from the specimens after the test finished. The photos of each of the specimens are shown in Fig.7 along with their respective failure modes of the UHPC infills. Two typical failure modes can be observed, namely shear failure and drum-shaped upsetting failure. In the case of shearing failure (D108T4CA15), two notable steel tube bulges can be observed near the supporting ribs at the two ends. The peeling paint in the diagonal zone indicates significant tilting deformation of the steel tube. On the concrete, a large diagonal crack is observed, coinciding with the location and the orientation of the diagonal zone on the surface of the steel tube and cutting the concrete into two parts. For the drum-shaped upsetting failure (D219T8CA00), small horizontal bulges appear close to the low end and around the steel tube. The concrete remains relatively intact, with only small vertical surface cracks.

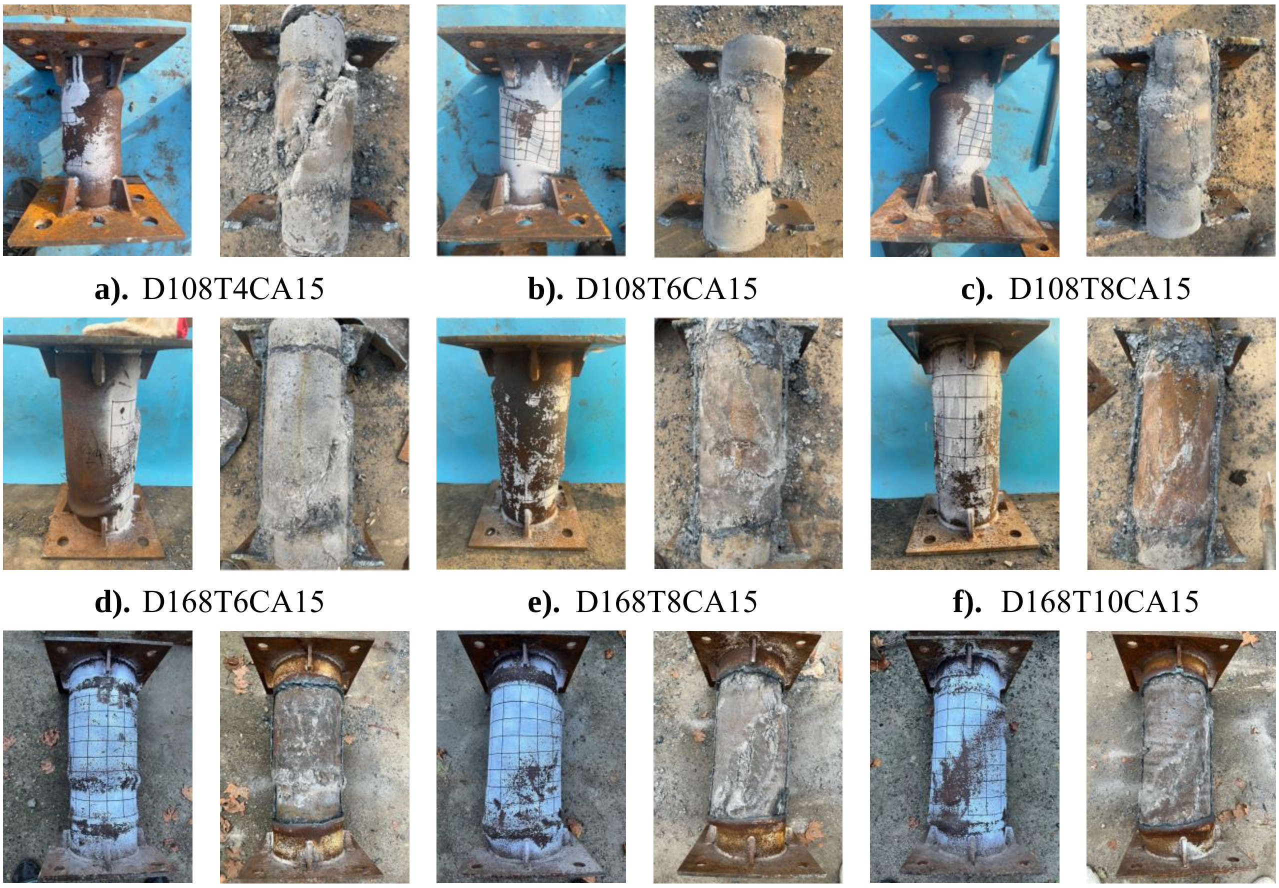

a). D108T4CA15 **b).** D108T6CA15 **c).** D108T8CA15

d). D168T6CA15 **e).** D168T8CA15 **f).** D168T10CA15

g). D219T8CA00 **h).** D219T8CA15 **i).** D219T8CA30

Fig.7. Photograph of failure modes for UHPCFSTs under axial compression

A strong correlation is observed between the failure modes and the design factors, such as steel tube thickness, steel tube diameter and coarse aggregate volume fraction of UHPC. As the steel tube thickness increases, as seen in the specimen groups D108T4CA15, D108T6CA15, D108T8CA15, D168T6CA15, D168T8CA15, and D168T10CA15, the confinement between the steel tube and the UHPCF increases. This leads to enhanced strength and deformation performance of the UHPC. Consequently, the failure modes of the specimens tend to switch from shear failure to drum-shaped upsetting failure. In specimen D108T4CA15, D168T6CA15 and D219T8CA15, the failure modes change with an increase in diameter while maintaining the same diameter/thickness ratio. Specimens with larger diameter tend to exhibit a closer resemblance to drum-shaped upsetting failure. With an increase in the coarse aggregate volume fraction of UHPC, as seen in specimens D219T8CA00, D219T8CA15 and D219T8CA30, the failure mode changes from drum-shaped upsetting failure to shearing failure. This can be attributed to the increased likelihood of cracking due to the presence of more coarse aggregate in the mixture.

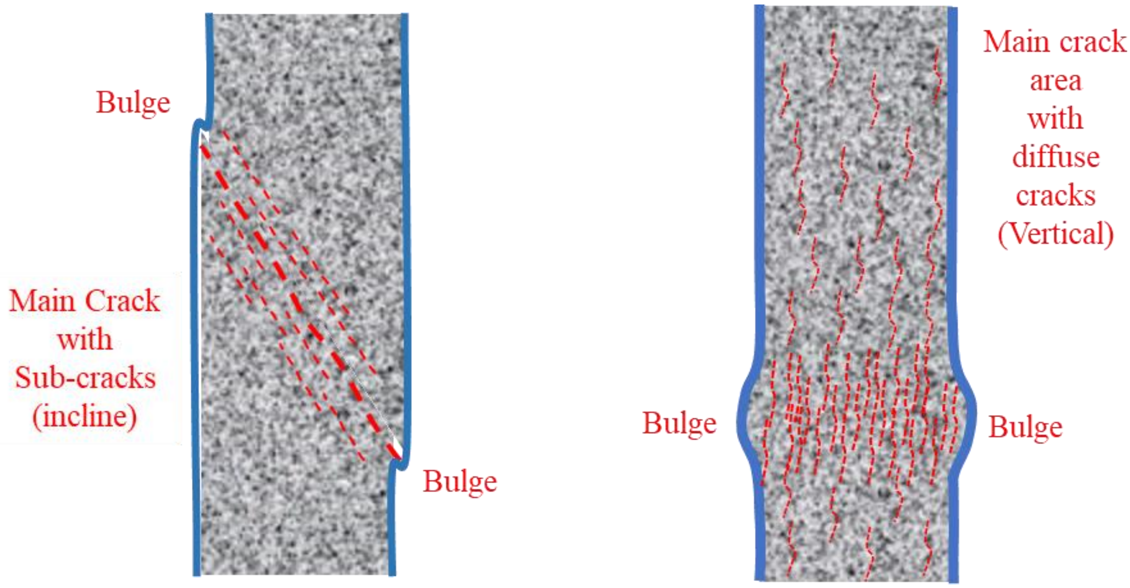

a). Shear failure at low confinement

b). Drum-shape upsetting failure at high confinement

Fig.8. Schematic diagram of failure modes for UHPCFSTs under axial compression

Based on the above analysis, it can be concluded that confinement is the primary factor influencing the failure modes observed in the UHPCFST under axial compression, seen in Fig.8. In previous research, Han proposed a confinement factor[30] that can quantitatively evaluate the level of steel confinement on the concrete in CFST structures. When the steel tube is thinner or the compressive strength of UHPC is higher, the specimens tend to exhibit shearing failure due to a lower level of steel confinement. As the level of confinement gradually increases, the failure mode of UHPCFST under axial compression changes from shearing failure to drum-shaped upsetting failure. The change of failure modes due to confinement is analogous to that observed in CFST structures. In additional, in comparison to normal concrete (NC), the increased strength of ultra-high-performance concrete (UHPC) requires thicker and higher-strength steel tubes for effective confinement.

3.2. Strain-force curve

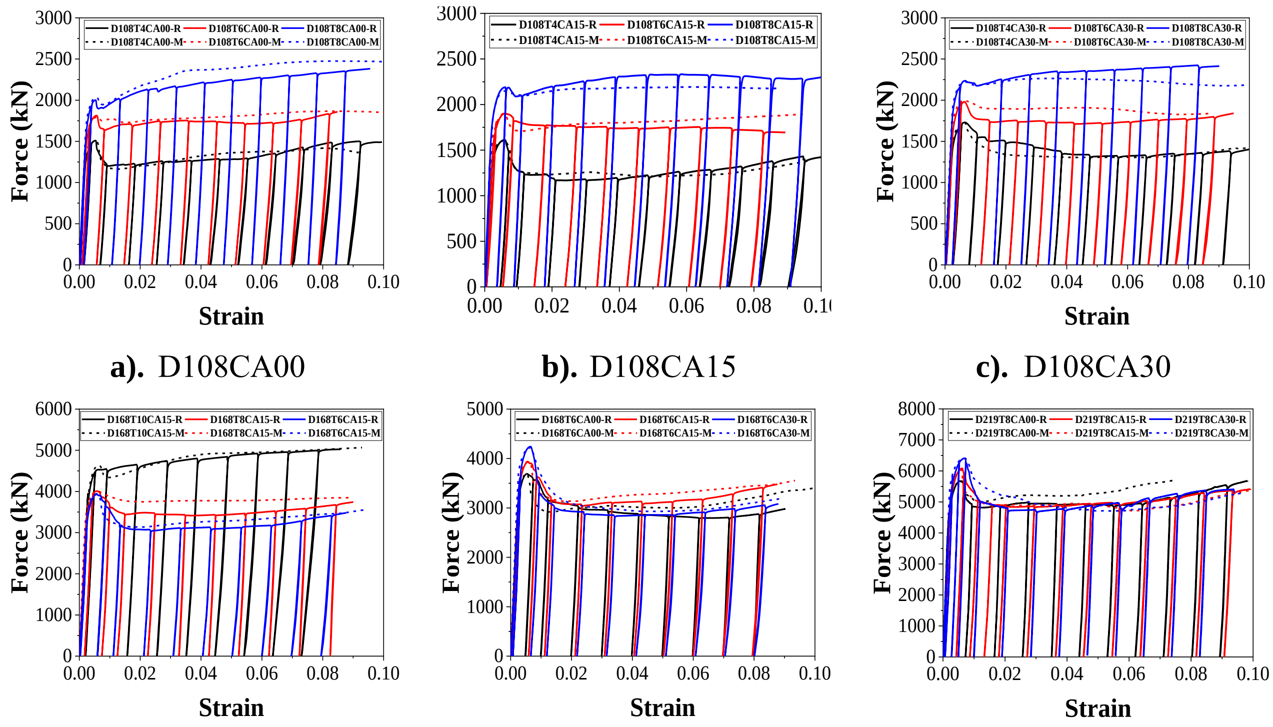

a). D108CA00 **b).** D108CA15 **c).** D108CA30

d). D168CA15 **e).** D168T6 **f).** D219T8

Fig.9. Strain-force curves of UHPCFSTs under monotonic and repeated compressions

The compressive force (N) applied to the specimens is plotted against the longitudinal strain (ε) in Fig.9. The N-ε curves of all the tested UHPCFST specimens exhibit similar characteristics. In the case of a specimen under monotonic compression, the curve initially shows an approximately linear phase until the steel tube yields. This is followed by an elastic-plastic stage until reaching the peak point. After the peak point, a descending phase occurs where the compressive force decreases as the strain increases. The descending extent of the force depends on the level of confinement between the concrete and the steel tube. Finally, a hardening phase is observed where the compressive force rises slightly until the compressive test end. For specimens subjected to repeated compression, the unloading and reloading stiffness of the specimens are noticeably smaller than the initial stiffness. Upon careful observation of Fig.9, it can be seen that the reduction in loading stiffness is less pronounced when the steel tube is thicker. This may be attributed to the reduced volume of concrete in the specimens with thicker steel. Furthermore, Fig.9 shows that the monotonic loading curves closely align with the load envelopes of the respective repeated compressive loading curves.

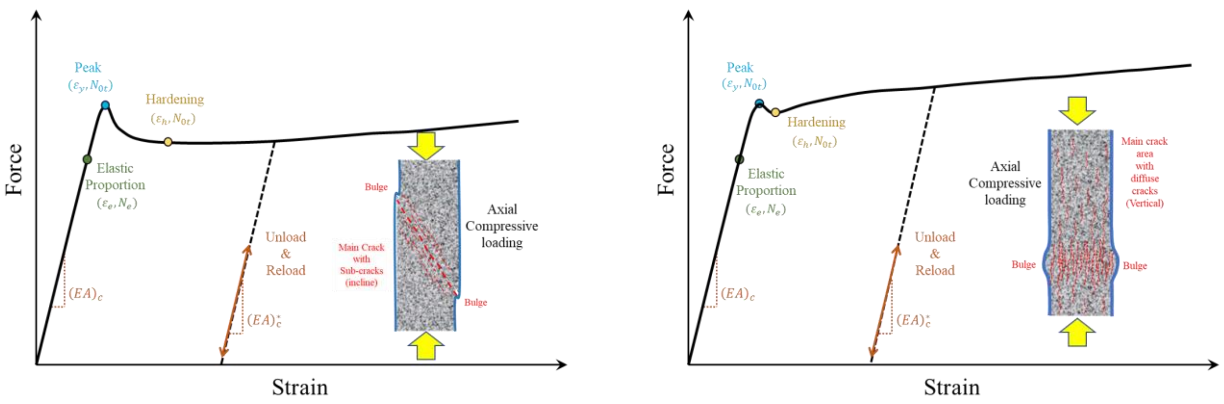

a). Low confinement **b).** High confinement

Fig.10. Typical load strain curves of UHPCFST under axial repeated compression

Fig.10 illustrates the typical N-ε curves of a UHPCFST under compression at different levels of confinement. The monotonic loading phase can be divided into four stages: linear, nonlinear, descending, and hardening. In the linear phase, the section elastic modulus $(EA)_c$ remains relatively constant, and the N-ε curve maintains linearity until the stress in the steel tube reaches its elastic proportional limit N_e, and the strain reaches the linear elastic limit strain ε_e. In the nonlinear phase, the steel tube starts exhibiting nonlinear properties with a gradual reduction in the tangle section modulus. When the compressive force reaches the peak compressive force (N_0), the strain reaches the yield strain (ε_y). As the displacement-controlled load continues to increase, the curve enters the descending phase. In this phase, the force starts to decrease while the strain increases. The descending extent of the force highly depends on the level of confinement, with higher confinement resulting in smaller force descending. In the hardening phase, the strain exceeds the hardening strain limit (ε_h), and the force increases at a rate much smaller than that of the elastic phase. It should be noted that for a UHPCFST with high steel confinement, the force may excess the peak force when the strain is large. For repeated compressive loading, the load-strain curves of unloading and reloading are nearly linear and identical. The unload and reload section modulus $(EA)_c^*$ are lower than the initial section modulus $(EA)_c$ due to the accumulated materials damage in the UHPCFST.

3.3. Analysis of the test results

3.3.1. Axial compressive bearing capacity

In this paper, axial compressive bearing capacity (N_0) of the UHPCFST subjected to compression is defined as the peak compressive force of the N-ε curve. Fig.11 shows the axial compressive bearing capacity of the UHPCFST specimens with different steel tube diameter, thickness and coarse aggregate volume fraction of UHPC. Regardless of whether it is monotonically or repeatedly loaded, with the increase in the thickness of the steel tube, the axial compressive bearing capacity of the UHPCFST increases significantly. The same relationship can be also found between axial compressive bearing capacity and coarse aggregate volume fraction. The ratios between the axial compressive bearing capacity of the monotonically and repeatedly loaded specimens are shown in Fig.11 c), which is close to one. This observation implies that the unloading and reloading process have little effect on the axial compressive strength of UHPCFST.

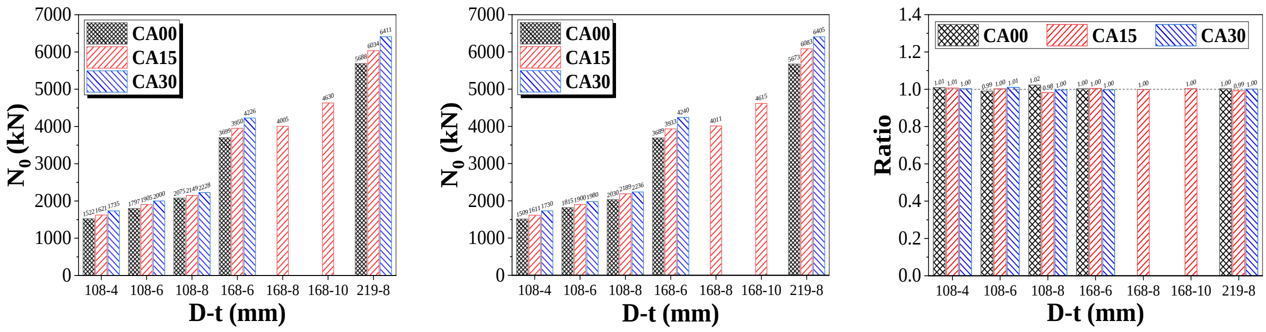

a). Monotonic loading **b).** Repeated loading **c).** Comparison between monotonic and repeated loading

Fig.11. Axial compressive bearing capacity of UHPCFST

To thoroughly investigate axial compressive bearing capacity of a UHPCFST, Strength Index (SI) is introduced and defined in Eq.(1), where N_0 is axial compressive bearing capacity of UHPCFST, f_y is yield strength of steel tube, A_s is sectional area of steel tube, f_c is cylinder compressive strength of UHPC and A_c is sectional area of UHPC.

$$SI = \frac{N_0}{f_y A_s + f_c A_c} \tag{1}$$

Fig.12 shows the relationships between the Strength Index (SI) and the confinement factor (ξ). It can be seen that the strength index increases with the increase of the confinement factor. The strength index shows a tendency to converge on a constant when the confinement factor rises high. When comparing the strength index of the UHPCFST of different diameters with similar diameter/thickness ratios, the specimens with larger diameters exhibit a lower strength index. Fig.12 also suggests the existence of an optimal confinement factor to achieve the highest strength index (SI). Nevertheless, due to the constraints related to UHPC production, steel tube procurement, and the maximum capacity of the testing machines, it is a current challenge for us to manufacture and test UHPCFST with very high confinement factors.

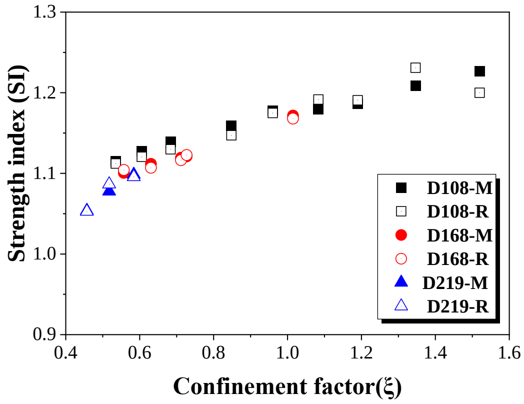

Fig.12. Strength index (*SI*) relationship with confinement factor (ξ)

3.3.2. Initial axial compressive stiffness

To evaluate the stiffness of a UHPCFST, a calculation method is proposed below. Fig.13.presents a typical unloading and reloading cycle, on which the tangent stiffness of the unloading and reloading paths is also calculated and shown. As seen from Fig.13., fluctuation and significant change of the stiffness occur in the region where the loading is about changing direction, at which the stiffness may be significantly lower due to plasticity or changes in the contacts between different material components. Thus, for consistency, only the middle 60% of the unloading and reloading path are used to calculate the tangent stiffness, i.e., in the range of 0.2P to 0.8P, where P is the force at which unloading starts. The linear regression method is used to establish a linear relationship between the force and the strain within the middle 60% of the data, from which the stiffness of the specimen can be determined. For calculating the initial stiffness, P is replaced by the force at yielding.

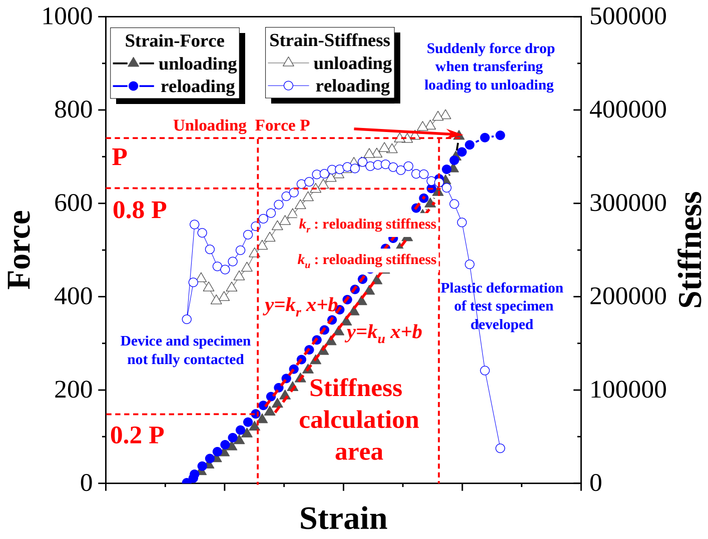

Fig.13. Stiffness calculation for unloading and reloading curve

This paper considers three types of stiffness: initial stiffness, unloading stiffness, and reloading stiffness. The initial stiffness is calculated from the ascending curve prior to yielding, and it applies to both monotonic and repeated loading. The unloading and reloading stiffness only apply to the repeated loading paths. In this section, the initial stiffness is analyzed to investigate the effects of some variables on the axial compressive stiffness. The other two types of stiffness, unloading and reloading stiffness, are primarily used to analyze stiffness degradation of the UHPCFST under axial compression.

The impact of the design variables of the specimen on the initial axial compressive stiffness is similar to its effect on the axial compressive bearing capacity, as illustrated in Fig.11 and Fig.14. As the thickness of the steel tube increases, the initial stiffness also increases due to a larger steel cross-sectional area. A Higher volume fraction of coarse aggregate UHPC leads to an increased elastic modulus of UHPC, consequently resulting in higher compressive stiffness of UHPCFST. When comparing the initial stiffness between UHPCFST under monotonic compression and repeated compression, the ratio of the initial stiffness of the two load patterns is approximately 1. This indicates that there is no significant additional effect on the initial stiffness due to the unloading and reloading process in the early stage of loading.

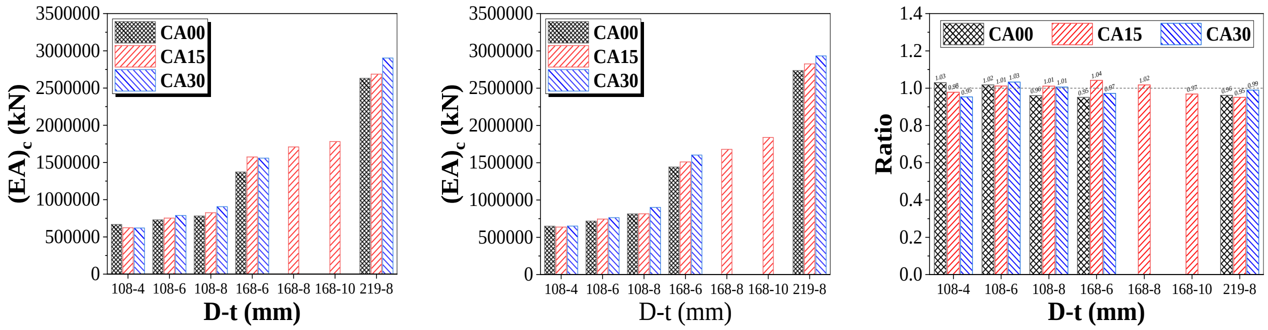

a). Monotonic loading **b).** Repeated loading **c).** Comparison between monotonic and repeated loading

Fig.14. Axial compressive stiffness of UHPCFST

3.3.3. Degradation of axial compressive stiffness

Damage to the materials of the UHPCFST occurs and cumulates during the loading process, which is manifested as a gradual attenuation of stiffness at a macroscopic level. The degree of stiffness attenuation is crucial for UHPCFST under seismic loads. In the repeated compressive load tests, it is possible to calculate the stiffness of the specimen under a given unloading strain, allowing for the study of stiffness degradation in UHPCFST subjected to axial compression.

As mentioned earlier, the unloading and reloading stiffness are primarily used here to analyze stiffness degradation. After carefully comparing the unloading and reloading stiffness for each unloading and reloading process, it is observed that the reloading stiffness is slightly greater than the unloading stiffness, with a difference of less than 5%. In this section, the reloading stiffness is utilized to analyze the axial compressive stiffness degradation of the UHPCFST under axial compression. Fig.15 illustrates the reloading stiffness for each unloading and reloading process of the test specimens under repeated compression. It can be observed that the specimens with thicker steel tubes exhibit higher stiffness throughout the loading test. For the specimens with different coarse aggregate volume fractions but the same steel tube thickness, it is observed that a higher proportion of coarse aggregate in the UHPC leads to higher stiffness at low strains. However, as the strain increases, the stiffness of the specimens with more coarse aggregate is reduced and eventually converges to almost the same value at the final stage of the loading process, as shown in Fig.15 b). The effect of tube diameters on stiffness degradation can be observed in Fig.15 c), where, for a fixed diameter-to-thickness ratio, the specimen with a larger diameter exhibits significantly higher stiffness throughout the entire test.

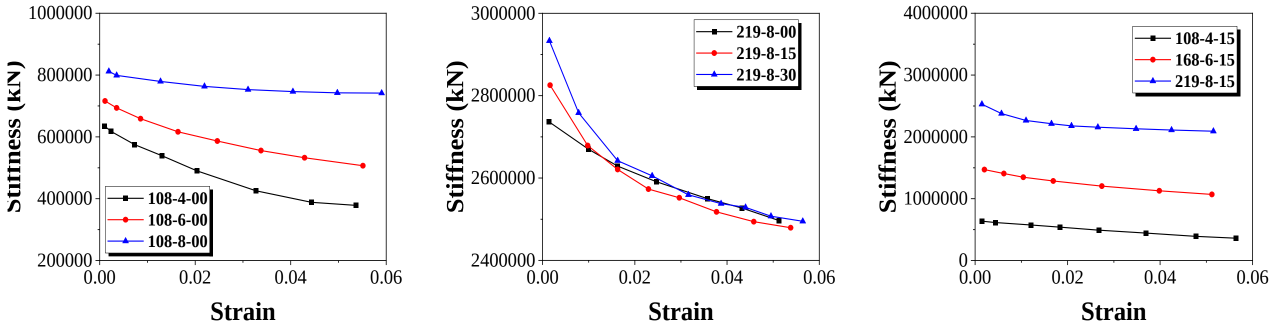

a). Thickness **b).** Coarse aggregate volume fraction **c).** Size

Fig.15. Compressive stiffness degradation

To further investigate stiffness degradation in the UHPCFST under compressive load, a stiffness reduction factor (D) is introduced. The factor D can be calculated using Equation (2), where $K_{unloading\{i\}}$ represents the reloading stiffness of the i-th unloading and reloading process, $k_{initial}$ represents the initial stiffness of the specimen.

$$D = K_{unloading\{i\}}/K_{initial} \tag{2}$$

Fig.16 illustrates the relationship between the stiffness reduction factor (D) and the unloading strain for repeated compressive specimens. It can be observed that tube thickness, coarse aggregate volume fraction, and steel tube diameter all have an impact on D. The specimens with thicker steel tubes show less stiffness degradation. This is because UHPC is more susceptible to damage than steel, and the specimens with thicker steel tubes have a lower proportion of UHPC, resulting in less damage. Regarding the coarse aggregate volume fraction, the UHPC with a higher proportion of coarse aggregate is more prone to cracking, indicating more damage within the material. The specimens with a lower coarse aggregate volume fraction demonstrate a less pronounced tendency of stiffness degradation. Fig.16 c) displays the relationship between stiffness degradation and tube diameter at the same steel ratio. When the unloading strain is less than 0.02, size has little effect on the stiffness degradation. However, when the strain exceeds 0.02, larger specimens exhibit less stiffness degradation. This observation is also supported by the fewer UHPC cracks observed in larger specimens at failure, as depicted in Fig.7.

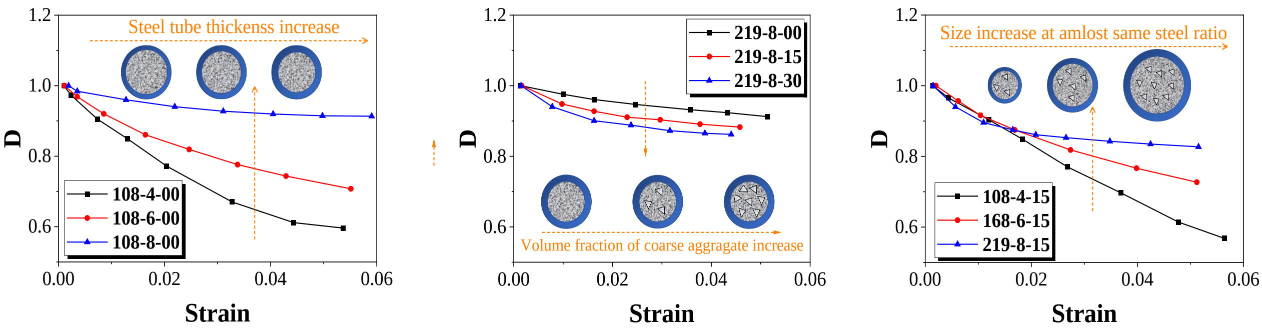

a). Steel Tube thickness **b).** V_{ca} **c).** Diameters

Fig.16. Compressive stiffness degradation for different variables

4. Calculation method of compressive mechanical performance of UHPCFST

4.1. Axial compressive bearing capacity

The axial compressive bearing capacity is considered the most important feature for the application of a CFST column. Numerous methods have been proposed for calculating the axial compressive bearing capacity of CFST, as summarized in Table.6.

Table.6 Commonly-used formulas to calculate axial compressive bearing capacity of CFST

Reference	Specimen type	Formulas	Notation
Liao[31]	UHPCFST	$N_0=\left(1+\alpha\frac{\xi}{1+\xi}\right)\left(A_c f_{ck}+A_s f_y\right)$	Upper bound for larger ξ
Lu[32]	UHPCFST	$N_0=\left(1+\left(4.18-0.50\lambda_{sf}\right)\frac{t}{d}\right)\left(A_c f_{ck}+A_s f_y\right)$	Using thickness ratio
Wu[27]	UHPCFST	$N_0=(1+1.33\,\xi)A_c f_{ck}$	Linear relation of ξ
Yu[33]	CFST	$N_0=\left(1+0.5\frac{\xi}{1+\xi}\right)\left(A_c f_{ck}+A_s f_y\right)$	Theory and experiment
Han[22]	CFST	$N_0=(1.14+1.02\,\xi)(A_s+A_c)f_{ck}$	Empirical

As mentioned in section 3.3.1. Size effect on the axial compressive bearing capacity of UHPCFST is not negligible, which is not taken into consideration in Table 5. The size effect on the axial compression bearing capacity of UHPCFST can be attribute to the size effect of UHPC, as presented by Wang[34–36]. Here, to consider the size effect in CFST columns, a strength reduction coefficient of concrete γ_u is proposed. The coefficient γ_u is defined as the ratio of the compressive strengths between the concrete with a diameter of d and the standard specimen, which is specimen with diameter of 168mm. The formula for axial compressive bearing capacity of UHPCFST that considers size effect can be then written:

$$N_0 = \left(1 + \alpha \frac{\xi_u}{1+\xi_u}\right)\left[A_c(\gamma_u f_{ck}) + A_s f_y\right] \tag{3-a}$$

$$\gamma_u = \left(\frac{d}{168}\right)^{0.11} \quad \xi_u = \frac{f_y A_s}{(\gamma_u f_c) A_c} \tag{3-b}$$

where ξ_u is the confinement factor that accounts for the size effect of specimens. γ_u is the adjustment factor for concrete strength due to size effect.

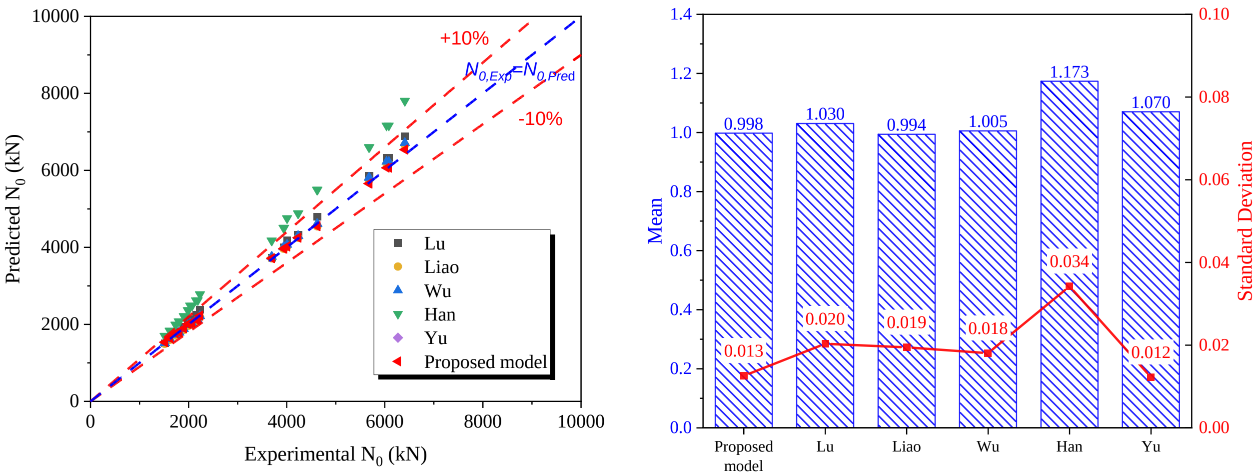

a). N_0 Prediction of existed and proposed models

b). Analysis of ratio between Predicted N_0 and Experimental N_0

Fig.17. Evaluations on models for axial compressive bearing capacity of CFST

Fig.17 shows the comparison between the prediction of the formulas in Table.6 and the experimental results on the axial compressive capacity of the UHPCFST. The predictions from the newly proposed formular (Eq.(3)) are also shown in the comparison. It can be found Han's and Yu's formulas both overestimate the capacity about 17.3% and 30.9%, respectively. The other three formulas in Table.6 agree well with the experimental results of this paper. Overall, the formula proposed in this paper that considers size effect presents the most accurate predictions.

4.2. Compressive stiffness and stiffness degradation of UHPCFSTs

Compressive stiffness of a UHCPFST is also an important mechanical property. The codes of practice of different regions and countries, such as CECS 28-2012 (CHN)[20], GB50936-2014(CHN)[19], ANSI/AISC 360-16(USA[37]), EC4(EU)[38], are all using the simple linear superposition formula to calculate the compressive stiffness of CFST, as shown in Equation (4).

$$(EA)_c = E_c A_c + E_s A_S \tag{4}$$

For the UHPCFST of this paper, a comparison of the predictions from Eq.(4) with the experimental results is made and shown in Fig.18. It can be found that this linear superposition formula can give a satisfied prediction on the initial stiffness of test specimens.

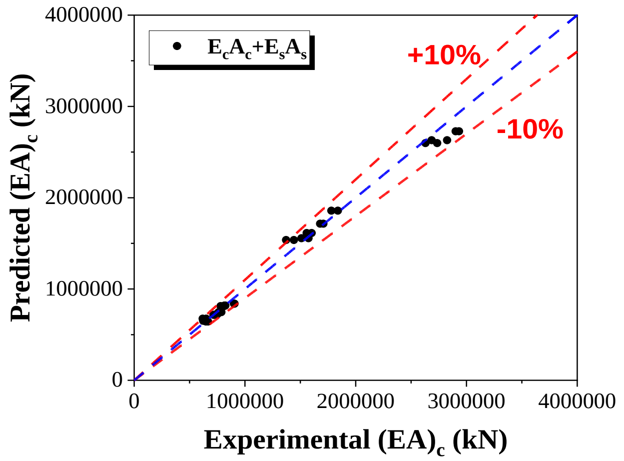

Fig.18. Compressive stiffness prediction of CFST

As discussed in Section 3.3.3, stiffness degradation is observed during the repeated axial compression tests of the UHPCFST. A stiffness reduction factor (D) was introduced to this effect. In practical applications, the Weibull distribution is commonly used to calculate failure probability of structures. In the context of this paper, stiffness degradation is considered as the macroscopic manifestation of micro-structural failure in the steel tube and UHPC. Therefore, the cumulative distribution function (CDF) of the Weibull distribution is selected to calculate the stiffness reduction factor. The original form of the CDF of the Weibull distribution is shown in Equation (5). In this study, a reliability function is defined in Equation (6) to calculate the stiffness reduction factor.

$$F(\varepsilon) = 1 - e^{-\left(\frac{\varepsilon}{\eta}\right)^{\beta}} \tag{5}$$

$$D(\varepsilon) = R(\varepsilon) = 1 - F(\varepsilon) = e^{-\left(\frac{\varepsilon}{\eta}\right)^{\beta}} \tag{6}$$

In Equations (5) and (6), ε represents the longitudinal strain of UHPCFST, while η and β are two constants specific to the UHPCFST specimen. The stiffness reduction factor, D, can be calculated using these three inputs. Section 3.3.3 provides a description of how the stiffness degradation varies with the thickness of the steel tube. To determine η and β, nine strain-force curves of repeated compression tests are utilized in curve fitting, resulting in the formulas in Equation (7). In this equation, d and t are steel tube diameter and thickness, respectively; α_{CA} denotes the coarse aggregate volume fraction of UHPC.

$$\eta = \frac{0.43}{0.002d - t + 7.9} \tag{7-a}$$

$$\beta = \frac{1}{\alpha_{CA} \cdot (0.001t^2 - 0.044) + 1.34} \tag{7-b}$$

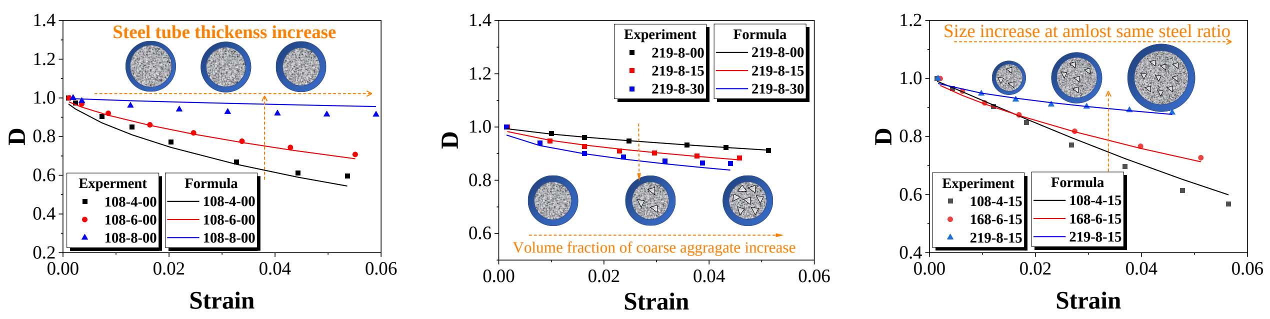

a). Steel Tube thickness **b).** V_{ca} **c).** Size

Fig.19. Prediction of proposed formula for stiffness reduction factor

Fig.19 demonstrates that the proposed formula (Eq.7) provides a relatively accurate prediction of the stiffness reduction factor (D).

4.3. Proposed model for load-strain curve

The load-strain response of UHPCFST under compression serves as a valuable tool for understanding the behavior of the component, predicting structural response, and optimizing UHPCFST designs. In this section, we construct an empirical load-strain curve for UHPCFST under compression.

4.3.1. Envelope curve

The empirical load-strain curve for UHPCFST comprises two parts: the envelope curve and the unload and reload path. The envelope curve is used to describe the mechanical behavior of the structural component under monotonic loads. As discussed in Section 3.2, a typical experimental strain-force curve for UHPCFST under monotonic compression consists of three phases, i.e., linear, nonlinear, softening, and hardening phases. However, for the purpose of simplification, the envelope strain-force curve neglects the nonlinear phase, seen in Fig.20. Therefore, the following formulas (Eq.8), are constructed.

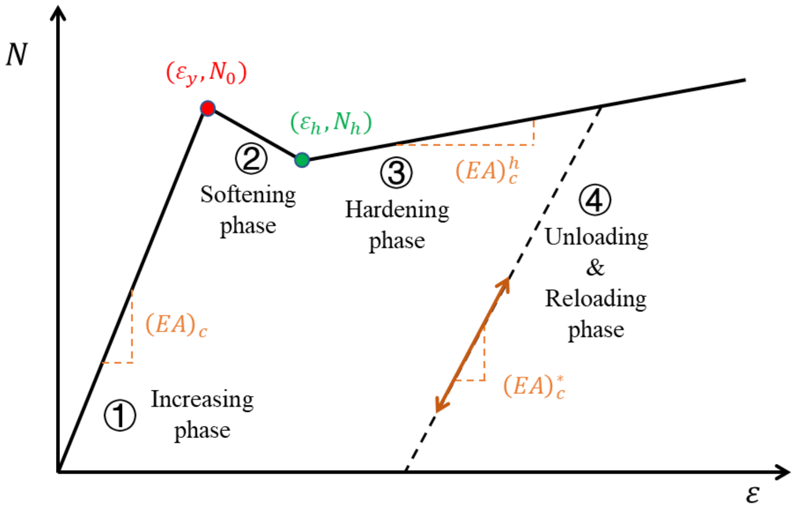

Fig.20. Schema diagram of empirical strain-force curve of UHPCFST under repeated axial compression

$$F = \begin{cases} (EA)_c \varepsilon & \varepsilon < \varepsilon_y \\ N_0 - (\varepsilon - \varepsilon_y)\dfrac{N_h - N_0}{\varepsilon_h - \varepsilon_y} & \varepsilon_y < \varepsilon < \varepsilon_h \\ N_h + \omega (EA)_c (\varepsilon - \varepsilon_h) & \varepsilon_h < \varepsilon < \varepsilon_u \end{cases} \tag{8}$$

For the elastic phase, a linear equation is appropriate until the strain exceeds the yield strain (ε_y). The section stiffness, $(EA)_c$, is calculated by Eq.(4), and the axial compression bearing capacity can be obtained from Eq.(9) below.

$$\varepsilon_y = \frac{N_0}{(EA)_c} \tag{9}$$

During the softening phase, where the strain is between the yield strain (ε_y) and the hardening strain (ε_h), the force decreases as the strain increases, and a linear relationship is applied. In the last phase of the envelope curve, namely the hardening phase, ω is used to describe the hardening modulus. By using the experimental data for regression, all parameters can be calculated based on the properties of the UHPCFST, as seen in Eq. (10) ~ (12).

$$N_h = (1 - \gamma) N_0 \tag{10-a}$$

$$\gamma = \left(\sqrt{\alpha_{ca}} + 1.933\right)e^{-15.4\alpha} \tag{10-b}$$

$$\varepsilon_h = \frac{1}{152.16 - \alpha(22.30\alpha_{\mathrm{ca}} + 8.97)} \tag{11-a}$$

$$\omega = 0.0005\left(\frac{1}{0.363 - \frac{\xi}{4}} + \alpha_{\mathrm{ca}}\right) \tag{11-b}$$

$$\varepsilon_u = 0.05 \tag{12}$$

4.3.2. Unloading and reloading curves

As discussed in Section 3.3.3, stiffness degradation was observed during the tests. Therefore, a linear model with progressively decreasing stiffness is used to characterize the unloading and reloading behavior of UHPCFST under repeated compression, as presented in Eq.(13). In this equation, F_{ul} represents the unloading force, and ε_{ul} denotes the unloading strain. The reduced section stiffness, $(EA)_c^*$, can be calculated using the original section stiffness, $(EA)_c$, and the stiffness reduction factor D introduced in Eq. (6) and (7).

$$F = F_{ul} - (EA)_c^*(\varepsilon - \varepsilon_{ul}) \qquad \varepsilon < \varepsilon_{ul} \tag{13-a}$$

$$(EA)_c^* = D(\varepsilon_{ul})(EA)_c \tag{13-b}$$

4.4. Load-strain model verification

Fig.21, Fig.22 and Fig.23 presents a comparison between the predictions of the proposed empirical strain-force model and the experimental data obtained from the monotonic and repeated compression tests conducted in this study. The strain-force model proposed in this paper is accurate in predicting the strain-force curves of the monotonic compression and the skeleton strain-force curves of the repeated compression tests. Furthermore, it also provides accurate predictions to the unloading and reloading curves observed in the repeated compression tests.

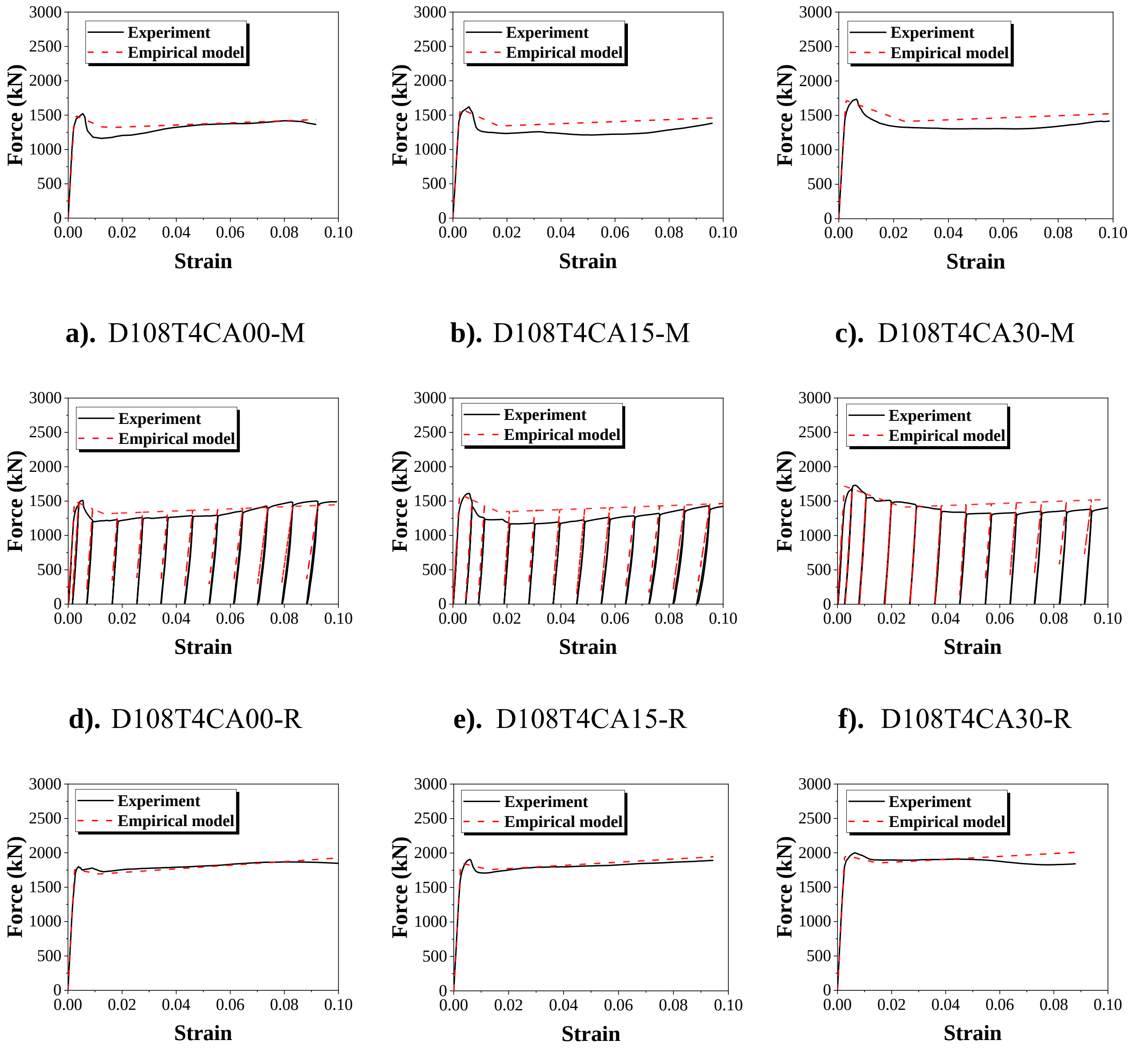

a). D108T4CA00-M **b).** D108T4CA15-M **c).** D108T4CA30-M

d). D108T4CA00-R **e).** D108T4CA15-R **f).** D108T4CA30-R

g). D108T6CA00-M **h).** D108T6CA15-M **i).** D108T6CA30-M

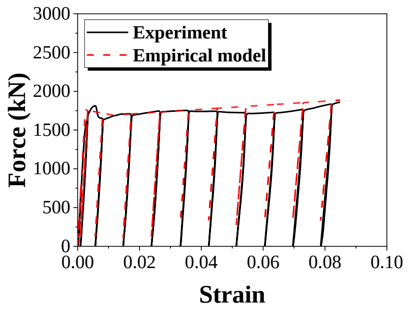

j). D108T6CA00-R **k).** D108T6CA15-R **l).** D108T6CA30-R

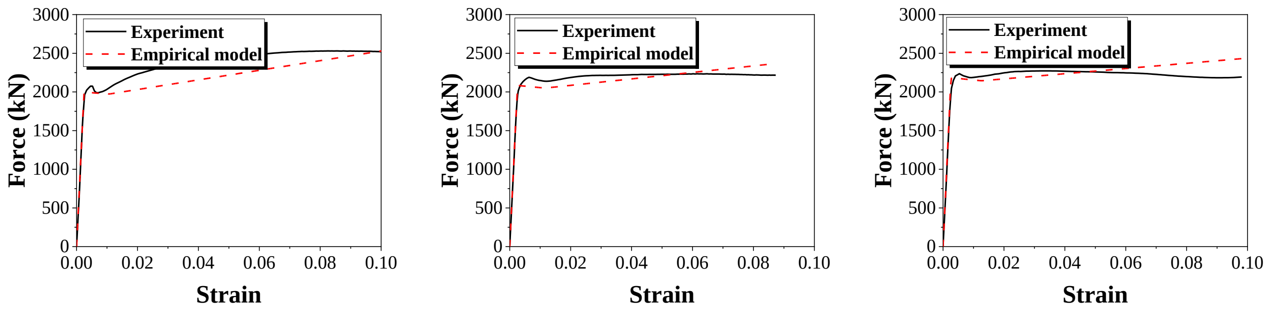

m). D108T8CA00-M **n).** D108T8CA15-M **o).** D108T8CA30-M

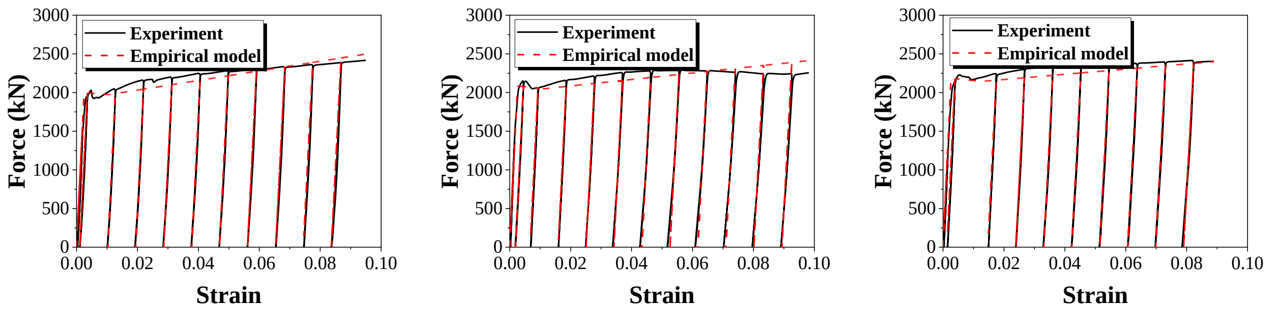

p). D108T8CA00-R **q).** D108T8CA15-R **r).** D108T8CA30-R

Fig.21. Prediction of proposed strain-force model on UHPCFSTs with 108mm diameters

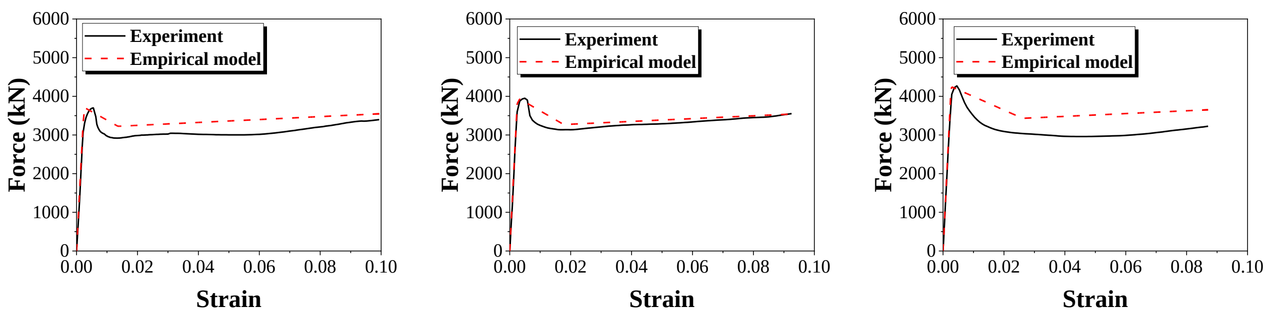

a). D168T6CA00-M b). D168T6CA15-M c). D168T6CA30-M

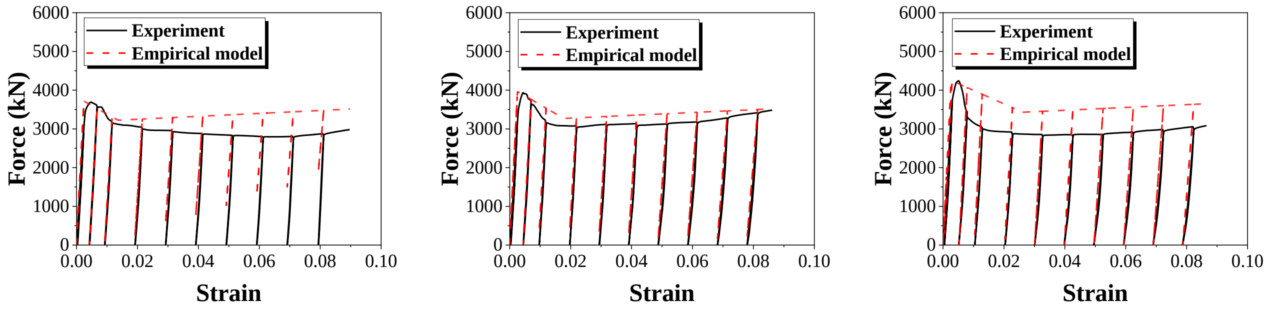

d). D168T6CA00-R e). D168T6CA15-R f). D168T6CA30-R

Fig.22. Prediction of proposed strain-force model on UHPCFSTs with 168mm diameters

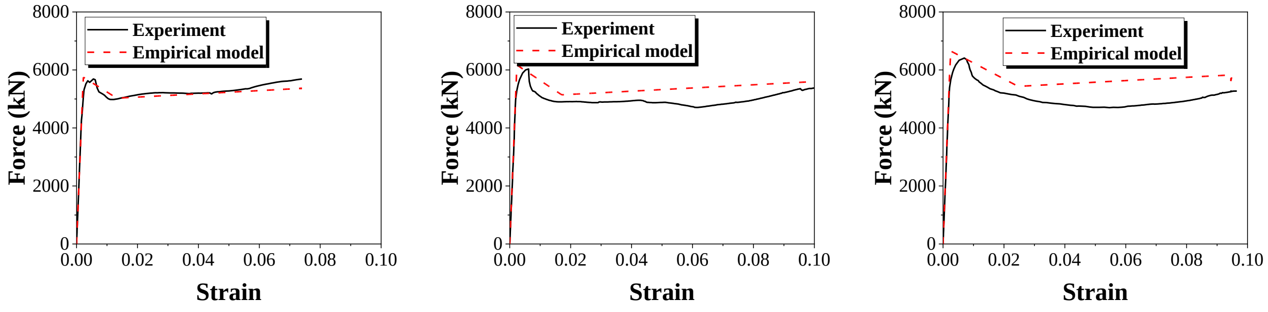

a). D219T8CA00-M b). D219T8CA15-M c). D219T8CA30-M

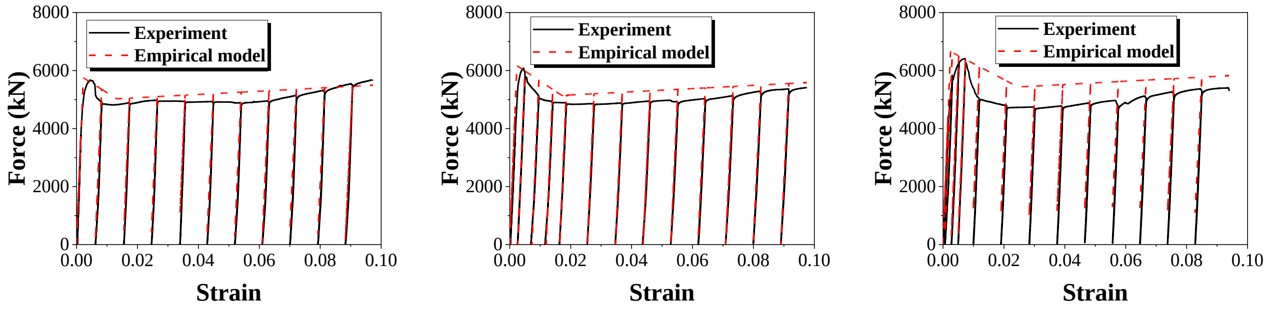

d). D219T8CA00-R e). D219T8CA15-R f). D219T8CA30-R

Fig.23. Prediction of proposed strain-force model on UHPCFSTs with 219mm diameters

To further verify the proposed strain-force models, experimental strain-force curves of the UHPCFST under compressive loads from Liao[31] are compared with the predictions of the proposed strain-force model. The details of the tested specimens, are presented in Table.7.

Table.7 Specimen design of Liao’s axial compressive UHPCFST experiments

Label	L	D	t	f_y	E_s	α_{CA}	f_c	E_c
108CA00	324	108	4	392.4	206	0	101	47
108CA15	324	108	4	392.4	206	15	114	48
108CA30	324	108	4	392.4	206	30	129	51
168CA30	504	168	6	366.6	205	30	129	51
219CA30	657	219	8	393.2	205	30	129	51

In Table.7, D, t and L denote, respectively, outside diameter, thickness and length of a steel tube; f_y is yield strength of steel; E_s is elastic module of steel; f_c is cylinder strength of concrete; α_{CA} is volume fraction of coarse aggregate of UHPC, E_c is elastic module of UHPC.

The comparisons are presented in Fig.24. It can be found that the proposed model can give a satisfactory prediction to the UHPCFST tested by Liao.

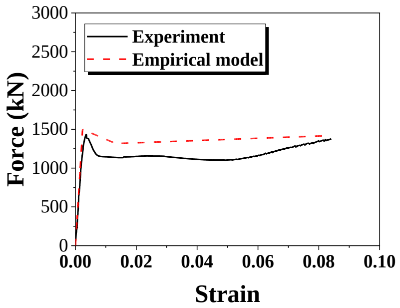

a). 108CA00

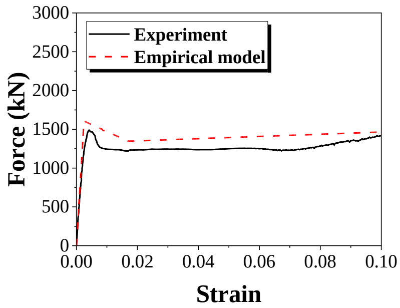

b). 108CA15

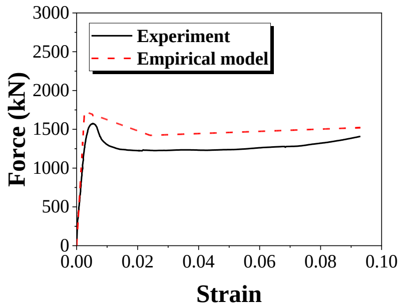

c). 108CA30

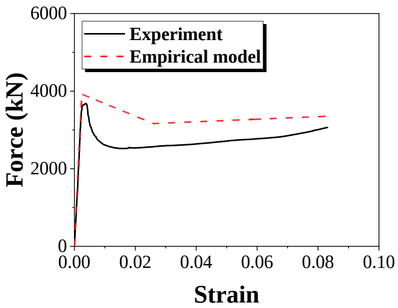

d). 168CA30

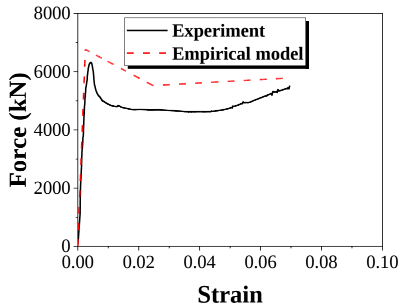

e). 219CA30

Fig.24. Prediction of proposed strain-force empirical model on Liao’s experimental curves

The discrepancies between the empirical model and the experimental results could be attributed to several factors. One possible factor could be the simplified assumptions made in the development of the empirical model, which may not fully capture the complexity of the mechanics of the UHPCFST. Additionally, experimental conditions such as measurement errors, environmental factors, or variations in the test setup could also contribute to the observed discrepancies.

5. Conclusion

In the present work, 34 UHPCFST specimens are tested under monotonic and repeated axial compression to investigate the compressive mechanical performance of the UHPCFST. Based on the results and discussions presented in this paper, the following conclusions can be drawn.

1) There are two different failure modes observed from the UHPCFST under axial compression, i.e., shear failure and drum-shaped upsetting failure. Specimens with low to high confinement factor present a failure mode transition from shear failure to drum-shaped upsetting failure.
2) The compressive bearing capacity significantly increases with the increase of steel tube thickness. The strength enhancement effect represented by the strength index (SI) increases with the increase of confinement factor of the UHPCFT. When steel ratio is fixed, an increase of steel tube diameter reduces SI value.
3) The load-strain curve of a UHPCFST under monotonic axial compression is close to the envelope of the load-strain curve of the UHPCFST under repeated axial compression, indicating that the accumulated strength degradation during the unloading and reloading process is limited.
4) The unload and reload strain-force curve of the UHPCFST under repeated axial compression

is almost linear. Stiffness degradation is observed, where the compressive stiffness decreases with the increase of strain. Steel ratio, coarse aggregate volume fraction and tube diameter all have impacts on stiffness degradation. Specimens with higher steel ratio, more coarse aggregates and smaller tube diameter present a more serious stiffness degradation.

5) The experimental results are used to evaluate the formulas proposed by Han, Yu, Wu, Lu and Liao. It is apparent that these formulas, which were originally proposed for CFST, overestimate the axial compressive bearing capacity of UHPCFST, while the newly proposed formulas in this paper show a good agreement with experiment results of this paper. To give a better prediction of axial bearing capacity of the UHPCFST, a formula that considers size effect is also proposed in this paper.

6) A simple three-phase empirical model is proposed to describe the load-strain curve of UHPCFST under compression. Moreover, evaluations of the proposed strain-force model are made using the experimental data from published literature. The proposed model can give accurate strain-force prediction for UHPCFST under axial compression. This model can be applied in practical design, analysis, and numerical calculations of UHPCFST.

Acknowledgments

This work was supported by the National Natural Science Foundation of China (Grant Nos. 52178157, 51738011). The last author is grateful to the Royal Society for supporting the research collaboration (IEC\NSFC\181449).

Reference

[1] Z. Dong, G. Wu, H. Zhu, X.-L. Zhao, Y. Wei, H. Qian, Flexural behavior of seawater sea-sand

coral concrete–UHPC composite beams reinforced with BFRP bars, Construction and Building Materials 265 (2020) 120279.

[2] J.Y. Zhu, F.X. Chen, X.Q. Dai, Y.Z. Tan, L.Q. Duan, Z.W. Zhang, Y. Leng, S.Y. Wang, T.Y. Yin, R. Yu, Development of a novel ultra-high performance concrete (UHPC) suitable for underwater operation: Design and performance evaluation, Journal of Building Engineering 75 (2023) 107030.

[3] Y. Su, C. Wu, J. Li, Z.-X. Li, W. Li, Development of novel ultra-high performance concrete: From material to structure, Construction and Building Materials 135 (2017) 517–528.

[4] D.-Y. Yoo, N. Banthia, Mechanical properties of ultra-high-performance fiber-reinforced concrete: A review, Cement and Concrete Composites 73 (2016) 267–280.

[5] N.K. Lee, K.T. Koh, S.H. Park, G.S. Ryu, Microstructural investigation of calcium aluminate cement-based ultra-high performance concrete (UHPC) exposed to high temperatures, Cement and Concrete Research 102 (2017) 109–118

[6] D. Zhang, Y. Liu, K.H. Tan, Spalling resistance and mechanical properties of strain-hardening ultra-high performance concrete at elevated temperature, Construction and Building Materials 266 (2021) 120961.

[7] M. Yu, W. Liao, S. Liu, T. Wang, C. Yu, S. Cheng, Axial compressive performance of ultra-high performance concrete-filled steel tube stub columns at different concrete age, Structures 55 (2023) 664–676.

[8] C.M. Tam, V.W.Y. Tam, K.M. Ng, Assessing drying shrinkage and water permeability of reactive powder concrete produced in Hong Kong, Construction and Building Materials 26 (2012) 79–89.

[9] F. Wu, L. Xu, Y. Zeng, M. Yu, B. Li, Behavior of CA-UHPC filled circular steel tube stub columns

under axial compression, Journal of Constructional Steel Research 211 (2023) 108204.

[10] D. Chen, X. Zha, P. Xu, W. Li, Stability of slender concrete-filled steel tubular X-column under axial compression, Journal of Constructional Steel Research 185 (2021).

[11] D. Chen, X. Zha, P. Xu, X. Zhai, Experimental and theoretical investigation of concrete-filled steel tubular x-column under axial compression, Journal of Constructional Steel Research 170 (2020).

[12] D. Chen, J. Wu, X. Zha, X. Hou, Study on selection of concrete-filled steel tubular X-column in large-scale cooling tower, Jianzhu Jiegou Xuebao/Journal of Building Structures 42 (2021) 322–331.

[13] K. Jani, P.V. Patel, Analysis and design of diagrid structural system for high rise steel buildings, in: Procedia Engineering, 2013: pp. 92–100.

[14] X. Han, C. Huang, J. Ji, J. Wu, Experimental and Numerical Investigation of the Axial Behavior of Connection in CFST Diagrid Structures, Tsinghua Science & Technology 13 (2008) 108–113.

[15] Q. Shi, W. Cai, B. Wang, Axial Cyclic Testing of Concrete-Filled Steel Tube Columns in Diagrid Structures, Advances in Civil Engineering 2019 (2019).

[16] Q. Shi, Y. Ying, B. Wang, Experimental investigation on the seismic performance of concrete-filled steel tubular joints in diagrid structures, Structures 31 (2021) 230–247.

[17] Z. Tao, B. Uy, L.-H. Han, Z.-B. Wang, Analysis and design of concrete-filled stiffened thin-walled steel tubular columns under axial compression, Thin-Walled Structures 47 (2009) 1544–1556.

[18] M.A. Bradford, H.Y. Loh, B. Uy, Slenderness limits for filled circular steel tubes, Journal of Constructional Steel Research 58 (2002) 243–252.

[19] CN-GB50936-2014: Technical code for concrete-filled steel tubular structures (press in Chinese),

(2014).

[20] CN-CECS 28-2012: Technical specification for concrete-filled steel tubular structures

[21] R. Bhartiya, D.R. Sahoo, R.M. Oinam, Cyclic axial stress-strain model for circular CFST columns under compression loading, Soil Dynamics and Earthquake Engineering 164 (2023) 107588.

[22] L. Han, Concrete filled steel tubular structures-theory and practice, Science, Beijing, 2007.

[23] M.-T. Chen, M. Pandey, B. Young, Post-fire residual material properties of cold-formed steel elliptical hollow sections, Journal of Constructional Steel Research 183 (2021) 106723.

[24] S. Yi, M.-T. Chen, B. Young, Stub Column Behavior of Concrete-Filled Cold-Formed Steel Semi-Oval Sections, Journal of Structural Engineering (United States) 149 (2023).

[25] S. Yi, M.-T. Chen, B. Young, Design of concrete-filled cold-formed steel elliptical stub columns, Engineering Structures 276 (2023) 115269.

[26] Metallic materials -Tensile testing - Part 1: Method of test at room temperature., 2010.

[27] F. Wu, L. Xu, Y. Zeng, M. Yu, B. Li, Behavior of CA-UHPC filled circular steel tube stub columns under axial compression, Journal of Constructional Steel Research 211 (2023) 108204.

[28] Y. Yan, L. Xu, B. Li, Y. Chi, M. Yu, K. Zhou, Y. Song, Axial behavior of ultra-high performance concrete (UHPC) filled stocky steel tubes with square sections, Journal of Constructional Steel Research 158 (2019) 417–428.

[29] T/CCPA 35—2022/ T/CBMF 185—2022 Specification for design of ultra-high performance concrete structures.

[30] Z.-B. Wang, Z. Tao, L.-H. Han, B. Uy, D. Lam, W.-H. Kang, Strength, stiffness and ductility of concrete-filled steel columns under axial compression, Engineering Structures 135 (2017) 209–

221. https://doi.org/10.1016/j.engstruct.2016.12.049.

[31] W. Liao, RESEARCH ON COMPRESSION PERFORMANCE OF ULTRA-HIGH PERFORMANCE CONCRETE FILLED STEEL TUBULAR COLUMNS AFTER HIGH TEMPERATURE DURING CONSTRUCTION, Wuhan University, 2023.

[32] L. Xu, Q. Lu, Y. Chi, Y. Yang, M. Yu, Y. Yan, Axial compressive performance of UHPC filled steel tube stub columns containing steel-polypropylene hybrid fiber, Construction and Building Materials 204 (2019) 754–767.

[33] M. Yu, X. Zha, J. Ye, C. She, A unified formulation for hollow and solid concrete-filled steel tube columns under axial compression, Engineering Structures 32 (2010) 1046–1053.

[34] Y. Wang, P. Chen, C. Liu, Y. Zhang, Size effect of circular concrete-filled steel tubular short columns subjected to axial compression, Thin-Walled Structures 120 (2017) 397–407.

[35] J. Wang, S. Ma, M. Cui, Numerical simulation of size effect in concrete-encased high-strength steel columns under axial compression, Structures 59 (2024) 105725.

[36] Chen P., RESEARCH ON SIZE EFFECT OF AXIALLY LOADED CIRCULAR CONCRETE-FILLED STEEL TUBULAR STUB COLUMN, Harbin Institute of technology, 2019.

[37] ANSI/AISC 360-16: Specification for Structural Steel Buildings, (2016).

[38] Eurocode 4: Design of composite steel and concrete structures Part 1-1: General rules and rules for buildings